Topologically induced confinement of collective modes in multilayer graphene nanocones measured by momentum-resolved STEM-VEELS

F. S. Hage,[1,2,3,*] Q. M. Ramasse,[1] D. M. Kepaptsoglou,[1] Ø. Prytz,[3] A. E. Gunnaes,[3] G. Helgesen,[2,3] and R. Brydson[4]

[1]*SuperSTEM Laboratory, SciTech Daresbury, Keckwick Lane, Daresbury, WA4 4AD, United Kingdom*
[2]*Physics Department, Institute for Energy Technology, NO-2027 Kjeller, Norway*
[3]*Department of Physics, University of Oslo, NO-0371 Oslo, Norway*
[4]*Institute for Materials Research, SPEME, University of Leeds, Leeds, LS2 9JT, United Kingdom*

In the expanding field of plasmonics, accurate control of the degree of plasmon localization is of crucial importance for tailoring optical properties at the nanoscale. In this paper, the degree of plasmon localization is directly probed by recording the momentum transfer dependence (i.e. the dispersion) of plasmon resonance energies using electron energy loss spectroscopy in the aberration-corrected scanning transmission electron microscope. Limited by the uncertainty principle, resolution in momentum space can easily be tuned by the beam convergence, and it is shown that localization is clearly identifiable, even at low-momentum resolution. In this proof-of-principle study, this technique was applied to multilayer graphene cones containing a varying number of topological defects at their apex. It is shown that a high degree of confinement of the π and $\pi + \sigma$ volume plasmons is reached for five pentagonal defects at the cone apex. This effect was attributed to the presence of the topological defects themselves. Furthermore, slight negative refraction was observed for the five-pentagon cone, predominantly affecting the collective excitation of the π electrons.

I. INTRODUCTION

In the rapidly expanding field of plasmonics,[1,2] the range of present and future applications is vast, including optical microscopy beyond the diffraction limit, ultrafast computing, molecular tweezers, highly efficient photovoltaics, and even invisibility.[2] The localization of electromagnetic energy in one or more dimensions is a key property in plasmonics since it affects strongly the optical response of single nanoparticles, planar wave guides, and plasmonic devices of more complex geometries. This allows for the design of devices able to trap and guide light at subwavelength scales, at predetermined frequencies.[1,2] The localization of electronic states is determined in real[1–3] or reciprocal space,[1,2,4–6] from their spatial or momentum transfer dependence, respectively. These properties can thus be probed for valence states (to which plasmonics are closely related) by exciting the devices by photons or electrons which undergo characteristic energy losses ($E < \sim 100$ eV).[1–3,5–9] In valence electron energy loss spectroscopy (VEELS), losses suffered by the incident electron radiation through its interaction with the sample are typically recorded in either a dedicated spectrometer or using a spectrometer attached to the column of an electron microscope.[3,7] As a direct result of the uncertainty principle, simultaneous high spatial and momentum resolution are mutually exclusive criteria for any given measurement.[10,11] Hence, spatially resolved studies have been the domain of the transmission electron microscope,[3] while momentum-resolved spectroscopy has been far less widespread and is conventionally carried out with a large parallel electron beam in a dedicated instrument.[5–9]

Despite being a relatively rarely used technique, a wide range of information is available from the momentum transfer dependence of energy loss spectra: e.g. identification of features due to retardation losses, band gaps, interband transitions, surface and volume plasmons,[12] as well as identifying local

changes in molecular orbital hybridization.[13] Examples of applications in the electron microscope include the mapping of defects in carbon nanotubes (CNTs),[13] the identification of guided light modes in graphite,[14] the investigation of the electronic structure of ZnO nanowires,[11] as well as the determination of dipole-forbidden transitions in $BaBiO_3$ (Ref. [15]) and NiO.[16] In this proof-of-principle study, the plasmon-loss/momentum dependence (or plasmon dispersion) is used to determine the degree of localization of the π and $\pi + \sigma$ volume plasmons in multilayer graphene cones and discs at high spatial resolution. In order to achieve high spatial resolution, the incident electron beam was converged, resulting in a subnanometer probe. The beam convergence puts a fundamental limit on resolution in momentum space, essentially creating a tradeoff between spatial and momentum resolution. The experimental conditions used here are thus both different and complementary to momentum-resolved electron energy loss spectroscopy (EELS) in the transmission electron microscope using a broad parallel electron beam, where much higher momentum resolution can be obtained at the expense of a poorer spatial resolution. A good example of the latter is given by Kinyanjui *et al.*,[17] who use a broad parallel beam (estimated to a diameter of <200 nm) to investigate the momentum-resolved dielectric response of graphene. While their experiment allows for accurate electron structure determination, it is unable to resolve and investigate the dielectric response of individual structural features at nanometer resolution, which is the goal of this paper.

Graphene nanostructures can be shaped into peculiar morphologies which result in topologically induced localized electronic states close to the Fermi energy. Such localized electronic states are thought to originate from the introduction of a number of topological defects in a sheet of graphene, a phenomenon originally predicted by theory[18,19] and confirmed by
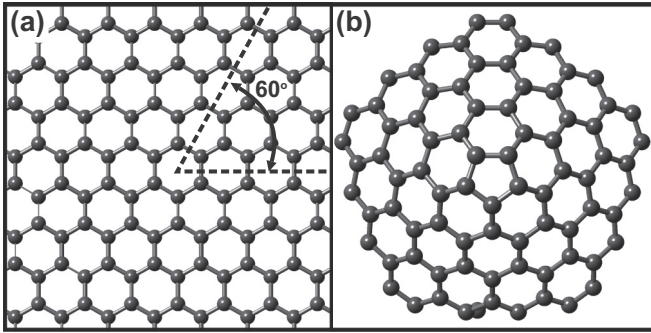
FIG. 1. (a) The formation of a $60°$ disclination in graphene, resulting in (b) a graphene cone with one pentagon at the apex.

experimental observations for a so-called graphene cone (with two pentagonal defects at its apex)[20] as well as for multiwalled CNTs capped by a structure comprising five pentagons.[21] Pentagons and heptagons are among the simplest of many possible topological defects in graphene[22–24] and consist of an atomic-scale rearrangement of the graphene lattice into a 5- or a 7-member carbon atom ring. More complex defects, often consisting of combinations of pentagons or heptagons, can be found e.g. as grain boundaries in the graphene sheet[22,25] or molecular junctions seamlessly connecting CNTs of different helicity.[26] When specifically introducing a number $P = 1–5$ of pentagons into a graphene sheet, it is possible to form a cone with a total disclination of $TD = P \times 60°$.[27] Figure 1 demonstrates how removing a $60°$ wedge [Fig. 1(a)] from the hexagonal graphene lattice and sewing the remaining edges of the sheet back together is consistent with the incorporation of one pentagon [Fig. 1(b)] in the lattice, thus forming a $60°$ disclination. Although single-layer graphene cones are yet to be observed experimentally at the atomic scale, Krishnan *et al.*[27] showed that industrially produced multilayer graphene cones exhibit characteristic apex angles $\xi = 180°$, $112.9°$, $84.6°$, $60°$, $38.9°$, and $19.2°$, which correspond to the theoretical apex angles of a graphene cone with zero (in which case it is referred to as a disc) to five pentagons at the apex, as given from Euler's theorem and symmetry considerations by $\sin(\xi/2) = 1 - P/6$.[27]

While in the multilayer case it is difficult to determine the exact number and type of topological defects at cone apices by direct imaging, the reported discrete cone apex angle values[27] unequivocally dictate the presence of a consistent number of pentagonal defects in each and every layer. Thanks to this unique structure, the number of atomic-scale topological defects at the apex of multilayer graphene cones is easily distinguishable by simply determining the macroscopic cone apex angle. As the topological defect concentration is predicted to have a large impact on the local electronic structure in graphene[22–24] and nanotubes,[21,26] graphene cones (and discs) offer a perfect model system for evaluating any of these effects on collective modes in multilayered carbon structures. For this purpose, three structures were chosen to represent a large number of defects ($P = 5$), an intermediate number ($P = 2$), and no defect at all (discs). Although the momentum resolution used in this study might result in slightly inaccurate electron structure determination,[10,11] it was found to be sufficient for the observation of two remarkable phenomena from π and $\pi + \sigma$

plasmon dispersions. For a large number of defects ($P = 5$), a high degree of localization and a slight negative refraction were identified, strongly indicating that the behavior of collective modes can be severely affected locally in structures where a high topological defect density is present.

The names π and $\pi + \sigma$ volume plasmons refer to the quasiparticle description of the resonant wave front resulting from of the collective excitation of either the π or all the valence electrons at characteristic energy losses $E_P = \hbar \omega_P$ and angular frequencies ω_P.[3,7] For plasmons, a localized state is characterized by a vanishingly small dispersion,[4,5] while delocalized states show a distinct band-structure-dependent dispersion,[5,6] which in the free-electron model can be shown to be parabolic.[3,7,28] A negative dispersion indicates negative refraction,[29] a property associated with metamaterials,[30,31] an exotic class of materials with applications in the design of perfect optical lenses and even cloaking devices.[2]

II. EXPERIMENTAL DETAILS AND METHODOLOGY

A. Sample preparation

Multilayer graphene cones and discs were fabricated by pyrolysis of crude oil with a plasma arc in the Kværner Carbon Black and Hydrogen Process (CB&H).[32] Subsequent graphitization was done by heat treatment at $2700°C$ in an argon atmosphere for 11 h in a graphitic kiln. The as-produced CB&H cones consist of a perfectly crystalline cone kernel enveloped by a thicker turbostratic nematic outer carbon layer. Only the cone kernel is expected to contain a well-defined number of pentagons at the apex. Upon heat treatment (at $2700°C$), this outer layer transforms into extended overlapping graphene layers with a significant variation in stacking order, thus deviating from a strict AB Bernal-type stacking.[33,34] Because of the multilayered crystalline structure after heat treatment, it is difficult to verify directly the presence of ordered pentagonal defects at the cone apex. However, the measured distribution of cone apex angles[27] separates in discrete values which correspond to the total disclination produced by the incorporation of up to five pentagons. This therefore dictates the presence of a consistent number of topological defects in each individual graphene layer. The presence of a random number of defects of various types would otherwise lead to the formation of a wide range of cone apex angles and certainly not the very specific distribution observed experimentally.

Microscopy specimens were prepared by sonicating particles suspended in ethanol and subsequently dispersing these onto a holey carbon grid. Only large freestanding areas of the cones and discs (i.e. areas overhanging a hole) were investigated in order to avoid any contribution of the amorphous carbon support film to the measured EELS signal. A slight influence of amorphous carbon was unavoidable as it was deposited in varying thickness on the sample. As graphene cones and discs exhibit a layer-upon-layer closed Russian-doll[35]-type structure with approximately semicircular curved edges,[33] disc edges were also avoided for analysis, so as to exclude any effect of curvature in the measured loss spectra.

B. STEM-EELS measurements

All measurements were carried out on a Nion Ul-traSTEM100 dedicated scanning transmission electron microscope[36] equipped with a Gatan Enfina EEL spectrometer. The microscope was operated at 60 kV in order to minimize irradiation damage to the carbon structures.[37] Convergence and collection semiangles were chosen as a function of the required momentum resolution, and off-axis EEL spectra were acquired by effectively displacing the spectrometer entrance aperture from the optical axis. Further details on experimental and theoretical aspects of momentum resolved scanning transmission electron microscope electron energy loss spectroscopy (STEM-EELS) measurements are given in the appropriate subsequent sections. Electron energy loss spectroscopy acquisition parameters were chosen in order to optimize the signal-to-noise ratio; 50 individual exposures were accumulated for each spectrum with a dispersion of 0.2 eV/channel. The dwell time was optimized for each acquisition, ranging from 0.1 s (on axis) to 2.0 s (off-axis). Long, averaged, dark current spectra were acquired and subtracted manually to minimize the influence of noise. This resulted in an effective energy resolution of 0.50 eV, as determined by the full width half maximum of the zero-loss peak (ZLP) feature present in all acquired EEL spectra.

Three structures were chosen to represent the full range of cone topological defect densities ($P = 0-2-5$), which will subsequently be referred to according to their number of apical pentagonal defects: a disc (P0), cone 1 (P2), and cone 2 (P5). Note, two different discs were investigated, where EEL spectra from one disc were acquired with $\alpha = 9$ mrad, while spectra from the other disc were acquired with $\alpha = 4$ mrad. This was done in order to assess the reproducibility of the measurements at different momentum resolutions. Henceforth, these discs will be referred to as disc 1 [P0(9 mrad)] and disc 2 [P0(4 mrad)].

Initial measurements of these nanostructures, done with a convergence semiangle of $\alpha = 9$ mrad, revealed significant differences in their plasmon dispersion. In order to evaluate the effect of increasing momentum resolution, $\alpha = 9$ mrad results were compared to measurements done at $\alpha = 4$ mrad, specifically comparing the topological extremes, i.e. differences between a flat disc with zero pentagons at the apex [P0(4 mrad)] and the five pentagon cone (P5).

C. Principles of momentum-resolved STEM-EELS

In EELS, the momentum transfer $\boldsymbol{p} = \hbar\boldsymbol{q}$ is given by the resultant scattered wave vector $\boldsymbol{q} = \boldsymbol{k}_1 - \boldsymbol{k}_0$, where $\boldsymbol{k}_0$ and $\boldsymbol{k}_1$ are the incident and scattered vectors, respectively.[3] The scattering angle θ relates to momentum space through

$$\boldsymbol{q}(\theta) = 4\pi \sin(\theta/2)/\lambda, \tag{1}$$

where λ is the electron wavelength. Equation (1) is easily derived from Bragg's law by $\boldsymbol{q}_{hkl} = 2\pi/\boldsymbol{d}_{hkl}$, where $\boldsymbol{d}_{hkl}$ is the real lattice spacing of the hkl plane. This scattering geometry is illustrated in Fig. 2(a), where the dashed circle indicates the circumference of the spherical spectrometer entrance aperture, which is positioned to exclude electrons with a scattering angle $\theta > \beta$ from contributing to the EEL spectrum.[3] Hence, the value of β, the collection semiangle,
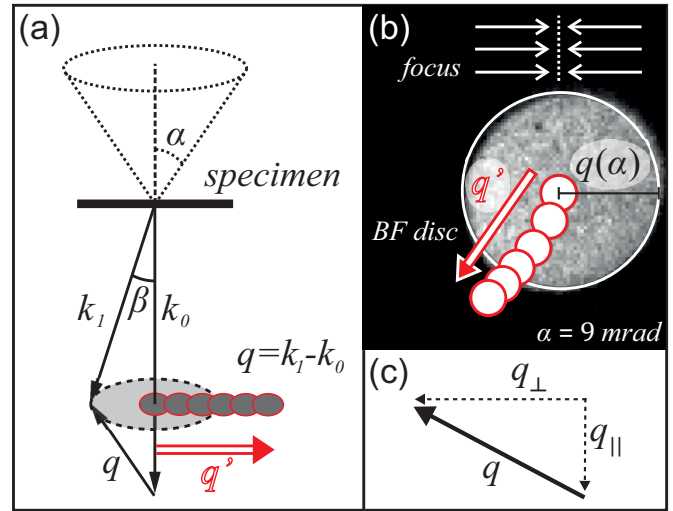

FIG. 2. (Color online) (a) Sketch of the scattering geometry, defining the momentum transfer in STEM-EELS. The darker circles indicate the effective off-axial shift of the spectrometer entrance aperture along $\boldsymbol{q}'$, at increasingly higher $\boldsymbol{q}$ values. (b) Image of the bright field (BF) disc projected onto the spectrometer CCD for $\alpha = 9$ mrad. The white discs show the displacement of the spectrometer entrance aperture along $\boldsymbol{q}'$ for measurements at increasingly higher $\boldsymbol{q}$ values [as indicated by the dark discs in (a)]. The focusing direction of the electron spectrometer is indicated. (c) Definition of the orthogonal components of $\boldsymbol{q}$: parallel and perpendicular to $\boldsymbol{k}_0$ in (a).

determines the resolution $\pm\boldsymbol{q}(\theta = \beta)$ if all incident electrons are parallel to the forward scattering direction [i.e. parallel to the $\boldsymbol{q}_\parallel$ component of $\boldsymbol{q}$, as defined in Fig. 2(c)]. In STEM mode, the electron beam is converged, which complicates the above situation by introducing incident wave vectors at an angle to the forward scattered direction $\boldsymbol{k}_0$. This is limited within a convergence semiangle α, defined by the probe-forming system (and the probe-forming aperture in particular). When $\alpha \geqslant 0$, the range of wave vectors allowed to contribute to an energy loss spectrum is significantly increased, resulting in a resolution $\pm\boldsymbol{q}(\theta = \beta^*)$, where $\beta^* = \sqrt{\alpha^2 + \beta^2}$ is the effective collection semiangle.[3]

Experimentally, resolution in momentum space was achieved by displacing the collection aperture along a vector $\boldsymbol{q}'$ relative to the optical axis represented by the six small overlapping discs in Figs. 2(a) and 2(b). This displacement was done by effectively projecting the center of the spectrometer entrance aperture off the optical axis, where the maximum range of $\boldsymbol{q}'$ was determined by electron-optical constraints. Momentum resolution was thus achieved by probing the inelastic signal parallel to $\boldsymbol{q}_\parallel$ [as defined in Fig. 2(c)], given that the direction of $\boldsymbol{q}'$ is normal to the spectrometer focusing direction,[38] which is indicated by white arrows in Fig. 2(b). A slight deviation from the latter criterion is shown in Fig. 2(b), which results in a decrease in momentum resolution.[38] However, this effect is assumed to be negligible compared to the impact of the beam convergence on the total resolution in momentum space.

Collection semiangle, resolution, and displacement in momentum space were thus calibrated from the image of the bright field disc projected onto the spectrometer CCD with the

TABLE I. Calibrated geometric scattering parameters, in units of Å^{-1}.

α,(mrad)	$\boldsymbol{q}(\alpha)$	$\boldsymbol{q}(\beta)$	$\boldsymbol{q}(\beta^*)$	Displacement along $\boldsymbol{q}'$
9	1.1	0.2	1.2	0, 0.4, 0.8, 1.0 1.3, 1.5
4	0.5	0.1	0.5	0, 0.2, 0.4, 0.5, 0.6, 0.8

entrance aperture removed. For a known convergence semiangle, the calibration is given by Eq. (1), i.e. the radius $\boldsymbol{q}(\theta = \alpha)$ of a circle superimposed on the estimated circumference of the slightly distorted image of the bright field (BF) disc in Fig. 2(b). These slight distortions are due to the fact that, in order to make the disc as round as possible (to facilitate the evaluation of convergence), the spectrum is defocused in the energy-dispersive direction using the spectrometer multipole optics. When the spectrometer entrance aperture was inserted, the radius $\boldsymbol{q}(\beta)$ and displacement along $\boldsymbol{q}'$ were given directly, and the resolution $\pm \boldsymbol{q}(\beta^*)$ was calibrated, resulting in the values shown in Table I. It thus follows that resolution in momentum space is $\pm \hbar \boldsymbol{q}(\beta^*)$, as given by the scattering geometry.

D. Spatial resolution

For a 4- or 9-mrad convergence semiangle, the electron probe size of the aberration corrected microscope[36] used in this study is mostly diffraction limited,[10] and if operated at 60 kV, the expected (real space) probe full width half maxima would be ~ 5 Å (4 mrad) and ~ 2.5 Å (9 mrad). Beyond the electron-optical resolution limit, delocalization of inelastic scattering imposes a physical limit on the spatial resolution obtainable in EELS.[3,10,39,40] Delocalization of inelastic scattering increases with decreasing energy loss and refers to the probability of exciting electrons a distance away from the position an incident electron impacts the sample. This can be quantified in terms of a localization diameter[41]

$$d_{50} \approx 0.8 \lambda (E_0/E)^{3/4}, \qquad (2)$$

within which 50% of inelastic scattering events occur. Here, E_0 is the incident electron energy, E is the energy loss, and λ is the incident electron wavelength. For 60-kV electrons, this yields localization diameters of ~ 4 and ~ 1 nm for the graphite in-plane π (7 eV) and $\pi + \sigma$ (28 eV)[42] plasmon losses, respectively. These values are in good agreement with recent delocalization estimates for plasmons at the edge of a graphene sheet by Zhou *et al.*[43] As delocalization lengths clearly exceed estimated probe sizes for either a 4- or a 9-mrad convergence semiangle, the spatial resolution of the π and $\pi + \sigma$ plasmon loss measurements in this work is estimated to $\cong 1$–4 nm, regardless of the resolution in momentum space.

E. Data processing

For an accurate determination of peak positions, the contribution of the zero-loss peak (ZLP) must be removed. While there is a large variety of ZLP removal techniques,[3,44] in the present case, the best compromise between noise levels and accuracy of the subtraction was obtained by removing the ZLP contribution using a power law fit to the ZLP
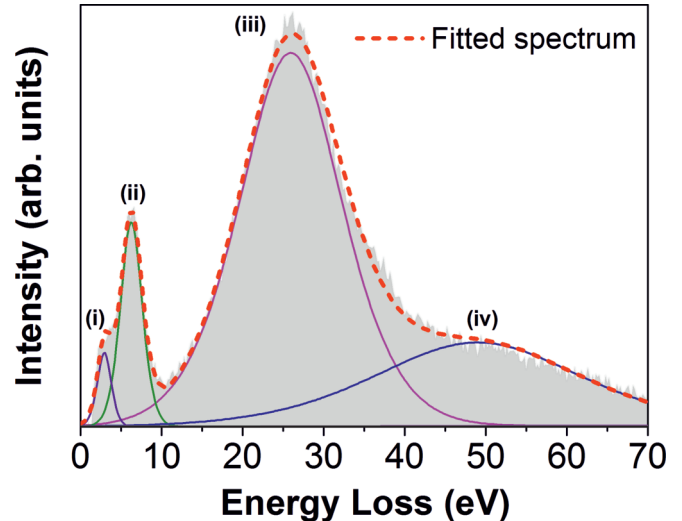

FIG. 3. (Color online) Example of peak fitting of the loss spectrum from cone 1 (P2), acquired with $\alpha = 9$ mrad and $\boldsymbol{q} = 0 \pm 1.2$ Å^{-1}. The contribution of the ZLP was removed by fitting of a power law. Peaks were attributed to (i) $\pi \to \pi^*$ interband transitions and possibly some residual intensity of the ZLP tail, (ii) a π plasmon, (iii) a $\pi + \sigma$ plasmon, and (iv) PS.

tail (see Appendix A for details). Plasmon peak positions were determined by fitting four components corresponding to: (i) $\pi \to \pi^*$ interband transitions; (ii) the π plasmon; (iii) the $\pi + \sigma$ plasmon; and (iv) plural scattering (PS), all on a linear background. Figure 3 shows an example of a fitted spectrum from the tip of P2 acquired with $\boldsymbol{q} = 0 \pm 1.2$ Å^{-1}, where components (i)–(iv) are indicated. Here, components (i)–(iii) were assigned following Ref. 45. Peak profiles were estimated using pseudo-Voigt functions, the only exception being spectra acquired at high $\boldsymbol{q}$ values (e.g. $\boldsymbol{q} = 1.3 \pm 1.2$ Å^{-1} and $\boldsymbol{q} = 1.5 \pm 1.2$ Å^{-1}), which due to significant peak broadening had to be fitted with asymmetric Lorentzians. This broadening is predominantly attributed to an expected increase in plasmon dampening with increasing momentum transfer.[46] Errors in fitted peak positions were estimated from statistics as well as from error in choice of peak shape, resulting in values of $\pm \sigma(E_\pi) \leqslant \pm 0.04$ eV and $\pm \sigma(E_{\pi + \sigma}) < \pm 0.15$ eV for the π and $\pi + \sigma$ plasmons, respectively. It should be noted that the real error in $\pi + \sigma$ plasmon peak position is expected to be significantly less than the estimated ± 0.15 eV maximum. A more detailed discussion of data processing and error estimation is given in Appendices A and B, respectively.

III. RESULTS AND DISCUSSION

A. Plasmon dispersion relations

In order to take advantage of the information available in momentum-resolved VEELS, the dielectric response of graphene cones and discs must be clearly understood. This is best done by comparing the present results on cones to literature on the closely related highly anisotropic electronic structure of Bernal stacked graphite. Thus, the sections below will show how cone and disc layer stacking disorder as well as topological defect concentration result in striking deviations
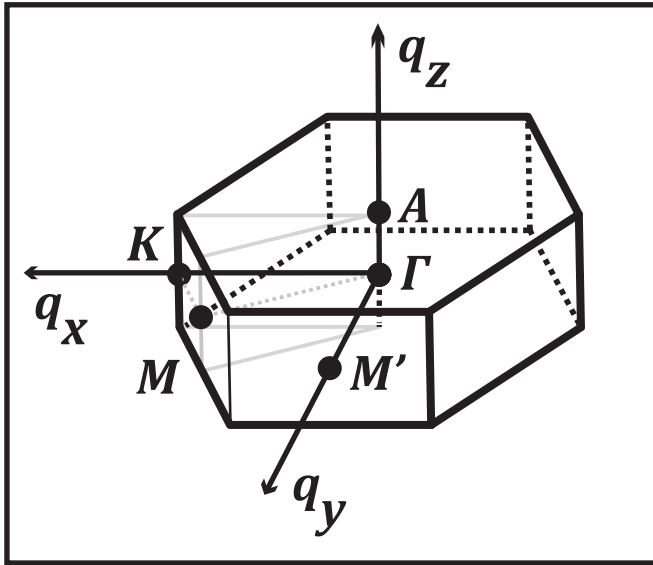
FIG. 4. Three-dimensional Brillouin zone of graphite. Gray lines are guides for the eye.

from the dielectric response of the purely sp^2 hybridized graphite system.

In the ideal case, graphite exhibits a perfect AB Bernal stacking of flawless graphene sheets, characterized by strong in-plane bonding and weak Van der Waals interplane interactions. The dielectric response is therefore dependent on the direction of $\boldsymbol{q}$, and it is thus necessary to describe the loss function (and the dielectric function ε) tensorially[7,47]

$$\text{Im}\frac{-1}{\sum_i \varepsilon_{ii}(\omega,\boldsymbol{q})q_i^2}, \tag{3}$$

where the subscript i denotes the coordinates of the orthogonal components of $\boldsymbol{q}$. Figure 4 shows the Brillouin zone of graphite, where the components $\boldsymbol{q_1} = \boldsymbol{q_x} \parallel \overrightarrow{\Gamma K}$, $\boldsymbol{q_2} = \boldsymbol{q_y} \parallel \overrightarrow{\Gamma M'}$, and $\boldsymbol{q_3} = \boldsymbol{q_z} \parallel \overrightarrow{\Gamma A}$ are indicated. In momentum-resolved EELS, electronic excitations are probed along the direction of $\boldsymbol{q}$ with a resolution dependent on the scattering geometry, as described above. In previous studies, a clear anisotropy of the dielectric response has been predicted[46,48] and measured[48,49,51] for momentum transfer along the $\overrightarrow{\Gamma K}$, $\overrightarrow{\Gamma M}$, and $\overrightarrow{\Gamma A}$ directions in the Brillouin zone. Thus, relative sample orientation must be taken into consideration for an accurate interpretation of the loss spectra. In the optical limit ($\boldsymbol{q} \to 0$), the situation can be simplified by the approximation $\varepsilon_x(E,0) = \varepsilon_y(E,0) = \varepsilon_\perp(E,0)$ and $\varepsilon_z(E,0) = \varepsilon_\parallel(E,0)$, where subscripts denote polarizations perpendicular (in-plane) and parallel (out-of-plane) to the crystallographic c axis of graphite.[7,51] Note that the approximation $\varepsilon_x(E,0) = \varepsilon_y(E,0) \neq \varepsilon_z(E,0)$ is not generally valid and is only used here in the special case of the dielectric response of graphite, given a range of momentum transfers relevant to the present results. As dipole selection rules are valid in the optical limit, the features in the in-plane component are assigned to a π (7 eV) and a $\pi + \sigma$ (28 eV) plasmon resonance as well as $\pi \to \pi^*$ ($E < 10$ eV) and $\sigma \to \sigma^*$ ($E > 10$ eV) interband transitions,[42,46,50] while the out-of-plane component is characterized by $\pi \to \sigma^*/\sigma \to$

π^* interband transitions[42,46,50] and a single $\pi + \sigma$ plasmon resonance at $\cong 18$ eV.[42] The contribution of each component to the resultant dielectric function is given in Ref. 8 as

$$\varepsilon(\omega,\varphi) = \varepsilon_\perp \sin^2 \varphi + \varepsilon_\parallel \cos^2 \varphi, \tag{4}$$

where φ is the angle between the crystallographic c axis and the direction of $\boldsymbol{q}$. The graphene cones and discs are multilayered structures, consisting of a number of overlapping extended graphene layers with a significant variation in stacking order along the crystallographic c axis, as seen for instance from electron diffraction of graphene cones[33,34] and discs.[33] Thus, neither cones nor discs conform to a strict single-crystal Bernal-type stacking. Despite this, the dielectric response of graphite is here used as a reference to evaluate the deviation of the measured loss spectra of cones and discs from the Bernal stacked graphite structure in terms of structural defects. Due to variations in cone and disc stacking order, it is thus assumed that the in-plane dielectric response of a multilayer structure can be approximated by a linear combination of the in-plane dielectric functions of graphite $\varepsilon_\perp(E,\boldsymbol{q}) = S\,\varepsilon_x(E,\boldsymbol{q}) + T\,\varepsilon_y(E,\boldsymbol{q})$, valid at any point in the $(\boldsymbol{q_x}, \boldsymbol{q_y})$ plane, where S and T are the fractional contributions of ε_x and ε_y as determined by the local structure. This closely resembles the situation in the optical limit, and the orientation dependence of a graphene disc can thus be expressed by simply including a $\boldsymbol{q}$ dependence in Eq. (4). For graphene cones this assumption is no longer valid as the graphene layers are curved, leading to an increased contribution of states along $\boldsymbol{q_z}$. However, if φ is redefined to be the angle between the direction of $\boldsymbol{q}$ and the effective orientation of the probed area of the cone projected onto a plane, a $\boldsymbol{q}$-dependent version of Eq. (4) should still apply.

In the simplest general case, the plasmon dispersion can be described by[3,7]

$$E_P(\boldsymbol{q}) = E_P(\boldsymbol{q_0}) + A\boldsymbol{q}^2, \tag{5}$$

$$A = (3/5)\hbar^2 E_F/m_0 E_P, \tag{6}$$

where $\boldsymbol{q_0}$ corresponds to the case of $\boldsymbol{q} \to 0$, E_P is the plasmon resonance energy, m_0 is the electron rest mass, and E_F is the Fermi energy. Equation (5) holds for $\boldsymbol{q} \ll \boldsymbol{q_F}$,[7] where $\boldsymbol{q_F}$ is the Fermi wave vector, while the dispersion coefficient in Eq. (6) corresponds to an idealized system which can be described by negligible plasmon dampening within the jellium model (i.e. free electrons).[3,7] This simple model breaks down at higher $\boldsymbol{q}$, which means that Eq. (5) can only be successfully applied to relatively small magnitudes of momentum transfer. For larger values of $\boldsymbol{q}$, Serra et al.[28] derived an expression within the extended random phase approximation

$$E_P(\boldsymbol{q}) = E_P(\boldsymbol{q_0}) + A\boldsymbol{q}^2 + B\boldsymbol{q}^4, \tag{7}$$

where the exact formulation of A and B depends on the electron density and dominant dampening mechanisms of the system, accounting for electron exchange correlation as well as band structure effects. In a way, Eq. (5) can be thought of as the special case of Eq. (7) where $B = 0$, valid only for low values of $\boldsymbol{q}$. Equation (7) agrees well with experimental data for high electron density alkali metals (e.g. Na), adhering to nearly free electron behavior even at $\boldsymbol{q} \geqslant \boldsymbol{q_C}$.[28] Within the jellium model,
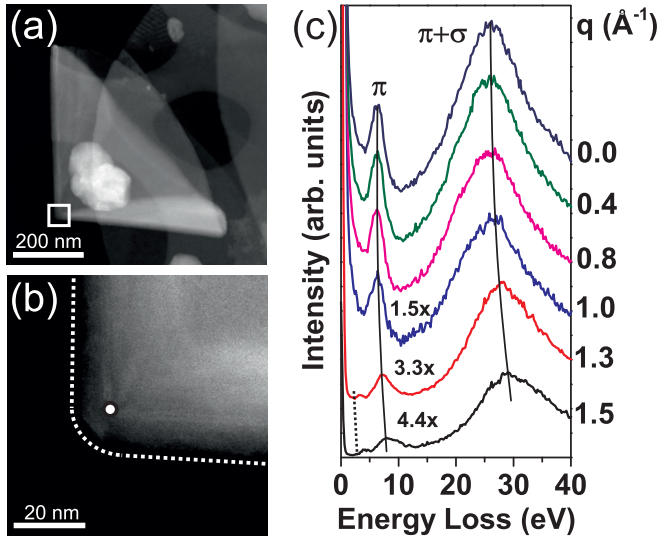
FIG. 5. (Color online) (a) HAADF STEM image of cone 1 (P2) with an extrapolated apex angle of 96°, corresponding to two pentagons at the tip. (b) The tip of the cone in (a). (c) Momentum-resolved loss spectra obtained from the apex of P2, showing a significant dispersion of the π and $\pi + \sigma$ volume plasmon peaks. This is mirrored in the approximated loss onset, indicated by the dotted line at high q values, the energy loss of which corresponds to a direct band gap transition. The beam position is indicated by a white disc with black circumference in (b). HAADF images and spectra were acquired with $\alpha = 9$ mrad. The white dashed line in (b) indicates the cone edge.

q_C is the cutoff wave vector corresponding to the momentum transfer $\hbar q_C$ necessary for exciting single electrons from the valence to the conduction band without transfer of momentum from the crystal lattice by phonons or through an Umklapp process.[3]

The effect of a finite collection semiangle has thus far been ignored, though it can be included by a convolution integral as described in Ref. [8]. This effect can be understood from Figs. 2(a)–2(c) and 4, where an increase in β results in an increased contribution of $q_\perp$, which for the simple case of k_0 parallel to q_z in graphite results in an increased contribution of q_x, q_y to the loss spectrum. In practice, the effect of a finite collection semiangle (in other words the momentum resolution) and the orientation dependence of the plasmon dispersion was found to be minor compared to that of local topology (i.e. the presence of defects). In fact, the effect of momentum resolution and orientation dependence manifested itself as slight changes in broadening and relatively small shifts in absolute energy losses. This broadening is attributed to an increased dampening of collective modes with increasing momentum transfer, the simplest case of which is well described in the jellium model.[3,7]

B. Cone and disc energy loss spectra characteristics

Prior to a quantitative analysis, the general characteristics of measured loss spectra from P0(9 mrad), P0(4 mrad) and P2, and P5 will be presented, exemplified by Figs. 5(c) and 6(c), respectively. Figure 5(a) shows a high-angle annular dark field (HAADF) image of P2 with an extrapolated apex angle of 96°,

corresponding to two pentagons at the tip. Here, the deviation from the 84.2° Euler angle[27] is attributed to measurement error, relative projection,[34] and possible imperfections in the structure.[33] The white disc marker in Fig. 5(b) indicates the position from which the momentum-resolved loss spectra in Fig. 5(c) were obtained: the beam was systematically placed at the center of the cone tip [Fig. 5(b)] at the expected position of the pentagonal defects, impinging both the outer graphene layers as well as the inner kernel.

These spectra were acquired with a convergence semiangle of 9 mrad, and corresponding scattering parameters are shown in Table I. Several important similarities with the q-dependent graphite loss spectrum[46,48,49,51] can clearly be identified in Fig. 5(c), indicating that, in spite of a significant deviation from a Bernal-type stacking, the dielectric response of the cone closely resembles that of graphite. With increasing q, a significant dispersion (i.e. an energy loss blueshift) and a distinct broadening of the high-energy shoulder of the π and $\pi + \sigma$ volume plasmon peaks[46,48,49,51] are observed, as well as an increase in the loss onset (i.e. the energy loss corresponding to a direct band gap), and a decrease in the relative ZLP intensity.[48,51] The approximate energy loss onset is indicated by the dotted line in Fig. 5(c) for the values $q = 1.3 - 1.5$ Å^{-1}. For $q < 1.3$ Å^{-1}, the lack of an observable loss onset was attributed to obscuring by the ZLP tail, while peak broadening was attributed to plasmon dampening: with increasing q, the oscillator strength of single-electron transitions is progressively shifted to higher energies as the electron screening is weakened,[46] resulting in a reduction in the plasmon oscillator strength following the conservation of the total oscillator strength as required by the Bethe sum rule.[3] Furthermore, for large q, the π plasmon is more efficiently dampened than the $\pi + \sigma$ plasmon in graphite, and for a cutoff wave vector $q_C \sim 1$ Å^{-1}, the π plasmon splits into a bimodal peak, for $q_y \parallel \overrightarrow{\Gamma M}$.[46] This is reflected in Fig. 5(c), where the π plasmon decreases more rapidly in intensity with increasing q than the $\pi + \sigma$ plasmon and shows a distinct asymmetric broadening at $q = 1.3 - 1.5$ Å^{-1}. All properties described above are observed in a similar manner in the momentum-resolved loss spectra of P0(9 mrad) and P0(4 mrad), not shown here.

Figure 6(a) shows a HAADF image of a cone (P5) with an extrapolated apex angle of 24°, corresponding to five pentagons at the tip, where the deviation from the theoretical 19.2° Euler angle[27] is again attributed to measurement error, relative projection,[34] and imperfections in the structure.[33] The white disc marker indicates the position from which the loss spectra in Figs. 6(c)–6(e) were obtained. These spectra were acquired with a convergence semiangle of (c) 9 mrad and (d) and (e) 4 mrad, where corresponding scattering parameters are shown in Table I. While broadening and a reduction of relative ZLP intensity in spectra in Fig. 6(c) are in qualitative agreement with those observed for P2 in Fig. 5(c), the π and $\pi + \sigma$ plasmon dispersions in Fig. 6(c) are vanishingly small for P5, in stark contrast to dispersions reported in the literature for graphite.[46,48,49,51] For $q = 1.3 - 1.5$ Å^{-1}, the loss onset (band gap) follows a similar behavior to the plasmons (i.e. little or no dispersion), as indicated by the dotted line in Fig. 6(c) drawn as a guide to the eye. This suggests a
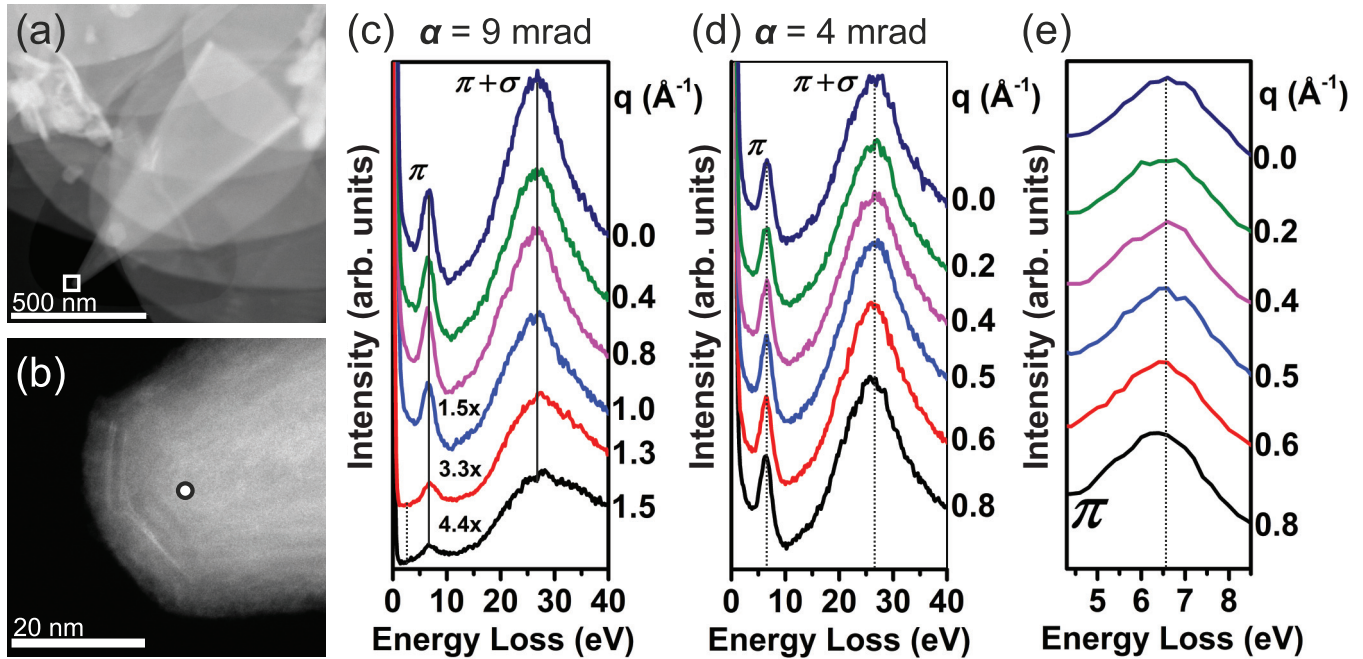
FIG. 6. (Color online) (a) HAADF STEM image of cone 2 (P5) with an extrapolated apex angle of $24°$, corresponding to five pentagons at the tip. (b) The tip of the cone in (a). Momentum-resolved loss spectra obtained from the tip of P5 with (c) $\alpha = 9$ mrad, and (d) and (e) $\alpha = 4$ mrad. The spectra in (c) show a vanishingly small dispersion of the π and $\pi + \sigma$ volume plasmon peaks. This is mirrored in the approximated loss onset, indicated by the dotted line at high q values, the energy loss of which corresponds to a direct band gap transition. However, for $\alpha = 4$ mrad, spectra show a slight negative dispersion of the (d) and (e) π and (d) $\pi + \sigma$ peaks. The beam position from which spectra in (c)–(e) were acquired is indicated by a white disc with black circumference in (b). HAADF images in (a) and (b) were acquired with $\alpha = 9$ mrad.

flattening of the band structure at the cone tip comprising a large number of topological defects and indicates a radically different electronic structure to that of graphite.[46] In fact, such a behavior is expected for highly localized states due to the reciprocity of real and momentum space. Indeed flattening of bands has been predicted at energies corresponding to localized topologically induced states in graphene.[25]

For the 4-mrad probe, the recorded loss spectra [Figs. 6(d) and 6(e)] show slightly negative dispersions of the π and $\pi + \sigma$ plasmon modes. This can be seen from comparing the changes in π [Fig. 6(e)] and $\pi + \sigma$ peak energies to the spectra acquired on the optical axis, indicated by the dotted vertical lines in [Figs. 6(d) and 6(e)]. In comparison to the 9-mrad measurements [Fig. 6(c)], spectra acquired with a 4-mrad probe [Figs. 6(d) and 6(e)] showed negligible broadening, and the loss onset was obscured by the tail of the ZLP for the more limited range of q (see Table I).

C. Experimental plasmon dispersions

Measurements of the plasmon dispersions are plotted in Fig. 7 ($\alpha = 9$ mrad) and Fig. 8 ($\alpha = 4$ mrad), where peak values were determined by the peak fitting routine detailed in the appendix. Due to the limited resolution in momentum space (especially for $\alpha = 9$ mrad) the absolute values of the plasmon dispersion constants are arguably not accurate enough for quantitative analysis. Thus, for $\alpha = 9$ mrad, Table II should be considered as a guide for comparative analysis between dispersion constants rather than an accurate measurement of

their absolute values. Nevertheless, this approach provides an excellent qualitative tool to compare the plasmon dispersions obtained from multilayer graphene cones of different topological defect densities. Furthermore, we note that, for $\alpha = 4$ mrad, the determined A_π of P0(4 mrad) agrees well with the value previously determined from graphite (to which P0 is closely related) at much higher momentum resolution.[7,51] This
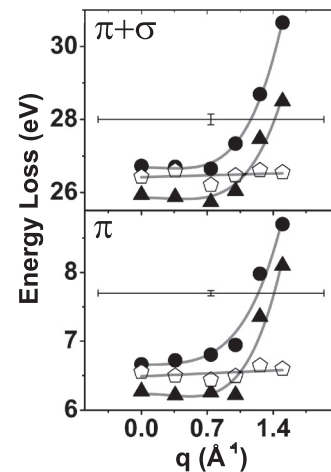

FIG. 7. ($\alpha = 9$ mrad) Dispersion of the π and $\pi + \sigma$ volume plasmons for P2 (▲), P5 (⬠), and P0(9 mrad) (●), fitted with Eq. (7) [P2, P0(9 mrad)] and a linear function (P5). Corresponding dispersion coefficients from Eq. (7) [P2, P0(9 mrad)] and from fitting Eq. (5) to the dispersion of P5 are listed in Table II.

TABLE II. ($\alpha = 9$ mrad) Plasmon dispersion coefficients of P2 and P0(9 mrad) [Eq. (7)] and P5 [Eq. (5)] from Fig. 7.

Topology (particle)	A_π (eV Å²)	$A_{\pi+\sigma}$ (eV Å²)	B_π (eV Å⁴)	$B_{\pi+\sigma}$ (eV Å⁴)
0 pentagons [P0(9 mrad)]	0.1 ± 0.3	-0.3 ± 0.2	0.4 ± 0.1	0.9 ± 0.1
2 pentagons (P2)	-0.3 ± 0.4	-0.3 ± 0.5	0.5 ± 0.2	0.7 ± 0.2
5 pentagons (P5)	0.05 ± 0.03	0.06 ± 0.08	n/a	n/a

shows that, notwithstanding the relatively modest momentum resolution used here, the absolute values of the plasmon dispersions measured at $\alpha = 4$ mrad could in fact provide a sound basis for comparison with literature values.

In Figs. 7 and 8, the difference in loss energies for $q \sim 0$ is attributed to local curvature, both in the sense of an orientation dependence on the plasmon energy[42] as well as changes in the local electron density given directly by the predicted[18,19] localized topology specific electron structure at apices of graphene cones. In terms of a pure orientation dependence, changes in the plasmon energy are attributed to an increased contribution to the loss spectrum of the $q_z \parallel \overrightarrow{\Gamma A}$ component[42] redshifting the plasmon energy in P2 and P5 compared to that of a flat disc [P0(9 mrad) and P0(4 mrad)], as described by the extended Eq. (4), all values being in the range of that of the graphite π (7 eV) and $\pi + \sigma$ (28 eV) plasmons.[42] Here, spectra from P0(9 mrad) and P0(4 mrad) were acquired with the incident electron beam oriented perpendicular to the disc surface.

The effect of increased momentum resolution between the $\alpha = 9$ mrad and $\alpha = 4$ mrad cases is observed as a reduction in spectral smearing, i.e. an averaging of spectral intensities from the range of momentum transfer values permitted to contribute to the recorded loss spectrum. Thus, upon increasing momentum resolution (by reducing the beam convergence from $\alpha = 9$ mrad to $\alpha = 4$ mrad), less of the intense spectral intensities from lower q values are permitted to contribute to the recorded off-axial loss spectra, which results in a more

distinct dispersion for an otherwise equal displacement of the collection aperture along q' [Figs. 2(a) and 2(b)]. This is easily seen by quantitatively comparing the π and $\pi + \sigma$ plasmon loss dispersions for P0(4 mrad) (Fig. 8) and P0(9 mrad) (Fig. 7), where (at similar values of momentum transfer) plasmon loss energies for P0(4 mrad) appear at significantly higher energies than those of P0(9 mrad). Regardless of the effect on absolute energy losses, the general trend in the plasmon dispersion was found to be less affected by changes in momentum resolution, showing significant dispersion for the discs while the dispersions of P5 remained vanishingly small.

Due to the rather large range of momentum transfers sampled in Fig. 7 (see Table I), it was found necessary to fit the dispersions of both the π and $\pi + \sigma$ plasmons from P0(9 mrad) and P2 with the extended Eq. (7), rather than the simpler Eq. (5). The fitted functions are shown as solid lines in Fig. 7, and corresponding dispersion constants are listed in Table II. Within the error of the polynomial fit, both yielded similar dispersions, with a small red-shift by $\Delta E_\pi(q_0) \approx 0.4$ eV and $\Delta E_{\pi+\sigma}(q_0) \approx 0.8$ eV from P0(9 mrad) to P2, which was attributed to the orientation dependence discussed above. As seen in Fig. 7, these shifts remain approximately constant for up to $q \sim 1$ Å^{-1}, indicating a significant dispersion of the polarization along $\overrightarrow{\Gamma A}$ and in qualitative agreement with the reported dispersion coefficient $A_\pi(\overrightarrow{\Gamma A}) = 2.8$ eV Å^{-1} [Eq. (5)].[51] For higher q, ΔE_π appears to decrease while $\Delta E_{\pi+\sigma}$ increases, which might indicate an increase in the π and decrease in the $\pi + \sigma$ plasmon dispersions along $\overrightarrow{\Gamma A}$. The small number of data points available at higher q as well as the relatively low momentum resolution makes an estimate of this effect less accurate, and further experiments might be needed to confirm this suggestion.

When using a 4-mrad convergence, a more limited range of sampled momentum transfers [than in the above case ($\alpha = 9$ mrad)] resulted in a satisfactory fit with Eq. (5) for the plasmon dispersions of P0(4 mrad). The use of the more extended Eq. (7) was therefore not necessary in this case. Thus, the dispersion coefficient A was given by the slope of $E_P(q)$ versus q^2 [Fig. 8(b)], where resulting values are listed in Table III. Here, A_π matches the graphite $A_\pi(\overrightarrow{\Gamma M}) = 3.3$ eV Å^{-1} for $q <\sim 0.7$ Å^{-1},[7,51] which was obtained at
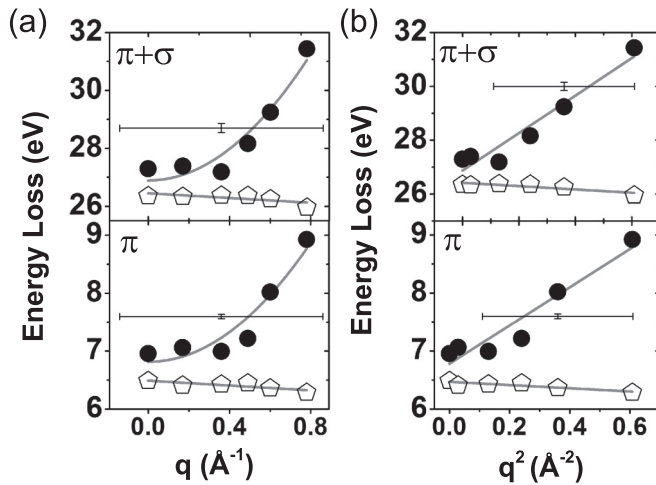

FIG. 8. ($\alpha = 4$ mrad) (a) Dispersion of the π and $\pi + \sigma$ volume plasmons for P5 (⬠) and P0(4 mrad) (●), fitted with a linear function and Eq. (5), respectively. (b) The dispersion in (a) is plotted against q^2 and fitted with a linear function, so the slope is the dispersion constant in Eq. (5), as listed in Table III.

TABLE III. ($\alpha = 4$ mrad) Plasmon dispersion coefficients [Eq. (5)] from Fig. 8(b).

Topology (particle)	A_π (eV Å²)	$A_{\pi+\sigma}$ (eV Å²)
0 pentagons [P0(4 mrad)]	3.3 ± 0.5	7.0 ± 0.9
5 pentagon (P5)	-0.6 ± 0.2	-0.3 ± 0.1

significantly higher momentum resolution,[51] indicating that a resolution of ± 0.5 Å^{-1} is sufficient for reasonable quantitative measurements. Note that the anisotropy[46,48,51] of the π plasmon dispersion in monocrystalline graphite along $\overrightarrow{\Gamma M}$ and $\overrightarrow{\Gamma K}$ (which should yield a slightly lower dispersion constant) could not be observed. The multilayer structure of P0(4 mrad) is assumed to cause significant peak overlap, averaging out any such peak separation. In all these cases, however, measurements showed a significant dispersion of the collective excitation of π and σ valence electrons, in good agreement with reported values for graphite.[5,46,48,51] This indicates a significant graphite-like delocalization of both π and $\pi + \sigma$ plasmons in P0(9 mrad), P0(4 mrad), and P2 [Figs. 7 and 8], in contrast to the highly localized behavior observed for these modes at the tip of P5 [Figs. 7 and 8].

We note that, due to the scattering geometry used here, the recorded energy loss response arises from a combination of loss events with momentum transfer lying potentially in any direction within the plane perpendicular to the optic axis. It is therefore not possible to directly identify any directionality of the plasmon response and determine, for instance, if the measured variations in q are mostly perpendicular or parallel to the cone tips [in the plane of both Figs. 5(a) & 5(b) and Figs. 6(a) & 6(b)].

Dispersion constants for P5 were calculated from Eq. (5) by the slope of $E_P(q)$ versus q^2 for both convergence semiangles, as shown for $\alpha = 4$ mrad in Fig. 8(b). Values listed in Tables II and III generally show a vanishingly small approximately linear dispersion of both π and $\pi + \sigma$ plasmons compared to those of P0(9 mrad) and P2, and P0(4 mrad). To further illustrate this point, a linear function was fitted to the dispersion of P5 in Figs. 7 and 8(a), showing good agreement with the data. Here, the effect of increasing momentum resolution is seen as a transition from what appears as a vanishingly small positive behavior to slightly negative values (see Tables II and III). This indicates a radical modification of the dielectric response at the tip of P5 compared to that characteristic of graphite.[5,46,48,51] In carbon nanotubes,[9] concentric shell fullerenes and C_{60} (Ref. 5) a reduced dispersion of π and $\pi + \sigma$ plasmon modes compared to that of graphite has been observed. For concentric shell fullerenes and C_{60}, this reduction has been attributed to partial and complete localization, respectively.[5] Similarly, in carbon nanotubes, orientation dependence of the π and $\pi + \sigma$ dispersions has been attributed to localization normal to the nanotube axis,[9] as postulated in Ref. 6. Thus, the vanishingly small dispersions of the π and $\pi + \sigma$ plasmons in P5 can be attributed to a pronounced localized behavior at the cone tip. This rather remarkable result can be rationalized in terms of topologically induced confinement of collective modes, the impact of which is postulated to increase as a function of cone apex defect density, as discussed extensively below.

D. Topologically induced plasmon confinement

For collective oscillations, localization can be understood by a simple set of arguments combining the jellium model of the dielectric response with classical wave mechanics. In the jellium model, the quasifree electrons in a material are displaced from their equilibrium position in response to an applied electromagnetic field, resulting in polarization. This will in turn set up a collective oscillation of the valence electron density at a characteristic angular frequency ω_P, an oscillation that can be quantized into wave packets and be described by a set of plasmon quasiparticles with an energy $E = \hbar \omega_P$.[3] From the definition of the group velocity $v_g = \nabla_q \omega$, it is clear that a vanishing $\omega - q$ dispersion corresponds to a standing wave with a zero-net wave packet velocity of propagation. Thus, a plasmon with a vanishing dispersion must be localized.

In a first approximation, it is assumed the slightly negative values of the P5 dispersion coefficients in Table III are ~ 0 (any implications of a slightly negative plasmon dispersion will be discussed later). Following this, the dispersion coefficients in Tables II and III indicate a localization of both π and $\pi + \sigma$ plasmons at the tip of P5, strongly suggesting a localization of all valence states. A standing wave model, as outlined above, has been reported to be a good first approximation for estimating energies of localized plasmons in metallic nanovoids[4] as well as in pyramidal pits.[52] It is important to note the term localization, as used here, refers to plasmon confinement and should not be confused with the energy-loss-dependent delocalization of inelastic scattering[10] as described by Eq. (2).[41] However, the degree of confinement might be related to the dependence of the inelastic delocalization on the type of electron excitation being probed, suggested by Zhou *et al.* for graphene.[43]

The origin of plasmon localization in P5 can be attributed to topology, i.e. to the effect of pentagonal defects on collective mode propagation and electron structure at the apex of P5. The discrete values of the graphene cone apex angles unequivocally dictate that their geometry is a result of the disclination produced in each individual layer by the incorporation of a consistent number P = 0–5 of topological defects. Whereas within the measurement error P0(9 mrad), P0(4 mrad), and P2 all showed π and $\pi + \sigma$ plasmon dispersions highly similar to those of Bernal stacked graphite; P5 showed by contrast a radical change in plasmon dispersion. Cones P0(9 mrad), P0(4 mrad), P2, and P5 all exhibit the same multilayer structure, the only significant structural difference between these particles being the presence of topological defects at the apices of P2 and P5. The high local topological defect density at the tip of P5, rather than any disorder in the multilayered structure (when compared to graphite), must thus be the origin of the observed confinement. This agrees with reports predicting that topological defects should have a large impact on the local electronic structure in graphene[18,19,22–24] and nanotubes,[21,26] and thus on their dielectric response. In this paper, this is observed as a confinement of collective modes at the apex of P5.

In following with this, the degree of localization is expected to increase with the number of topological defects in graphene cones, and for a sufficient defect density, confinement is achieved. From the π and $\pi + \sigma$ plasmon dispersions of P5 (Figs. 7 and 8), it can be concluded that a defect density of five pentagons in relatively close proximity at the apex of the cone[18,19,21,27] appears to be sufficient for achieving localization. By contrast, the plasmon dispersions of P2 are similar to those of P0(9 mrad), indicating significant plasmon propagation. Hence, a two-pentagon topology appears to be

insufficient for any significant degree of localization. However, a partial localization cannot be excluded altogether, as the dispersions of P2 might show differences to those of P0(9 mrad) at sufficiently high momentum resolution and exhibit behavior akin to the more highly defected case of P5.

Going beyond a simple collective model, it must be recognized that, with increasing q, collective modes experience increased dampening. This is predominantly attributed to transfer of momentum and energy to single electron transitions.[3] Thus, the collective character attributed to the measured π and $\pi + \sigma$ peaks is expected to decrease with increasing momentum transfer, attaining progressively the character of band-structure-dependent single electron excitations.[3] In light of the measured plasmon dispersions, this indicates a significant flattening of the band structure of P5 at higher q, in stark contrast to results from P0(9mrad), P0(4 mrad), and P2, as well as graphite.[46] This fits well with the prediction of a flattening of the band structure at energies corresponding to localized topologically induced states in graphene,[25] as well as the above-estimated vanishing dispersion of the loss onset at higher momentum transfers in Fig. 6(c).

Finally, based on the above discussion of localization, it is possible to put forward an interpretation of the effect of the possibly slightly negative dispersion observed at the tip of P5. When carrying out the measurements at higher momentum resolution ($\alpha = 4$ mrad), the measured value of A_π for P0(4 mrad) agreed particularly well with the reported $A_\pi(\overrightarrow{\Gamma M})$ of graphite,[7,51] thus improving upon the 9-mrad measurements in this study. This agreement, admittedly in the case of a flat disc [P0(4 mrad)], could be taken as a justification for tentatively interpreting the reduction from near-zero to a slightly negative dispersion for P5 on improving the momentum resolution as a real physical effect rather than attributing this solely to experimental error. Again, considering a plasmon as the envelope of the undamped collective oscillation of valence electrons, a negative dispersion would correspond to a transport of energy in a direction antiparallel to the direction of the transferred momentum. In more simple terms, this indicates a negative group refractive index. Such behavior is characteristic[29] of a class of materials known as metamaterials,[30,31] wherein negative refraction at visible frequencies has been observed by optical excitation of a surface plasmon wave guide.[31] Similar observations were made for bundles of silver nanowires.[30] Applying this model to the dispersion coefficients of P5 in Table III, it can be suggested that, in addition to a substantial degree of confinement in P5 as compared to P0(9 mrad), P0(4 mrad), P2, and graphite, negative refraction might be a native feature of the electron structure at the cone tip. In contrast to measurements of P0(4 mrad), $|A_\pi| > |A_{\pi+\sigma}|$ for P5 (see Table III). Negative refraction would thus primarily affect the collective oscillation of π electrons. This conclusion would be in good agreement with the fact that a negative group velocity is predicted for the π plasmon of AA stacked graphite in the case of significant contribution of $q_z \parallel \overrightarrow{\Gamma A}$ to the loss function,[53] an effect attributed to band structure. A similar explanation might be expected in the case of P5. The larger impact of negative refraction on π electrons might be understood from their weakly bound character in graphite and related carbon structures. While any technological implication

of a topologically induced negative refraction in graphitic materials is unclear at this time, the effect could possibly lead to interesting applications in novel plasmonic devices.

IV. CONCLUSION

In examining the momentum transfer dependence of valence electron excitations in the scanning transmission electron microscope, the degree of localization was determined for individual modes in graphene cones and discs. Specifically, the collective excitations of π and $\pi + \sigma$ electrons were found to be confined at the tip of a graphene cone with a topology corresponding to five pentagonal defects at its apex, while flat discs and a cone with only two pentagons at the apex exhibited a delocalized graphitic character. By extension, this suggests that the degree of collective confinement could directly be tailored by controlling the number and relative position of topological defects in graphene. In addition, a slight negative dispersion was tentatively identified for the five-pentagon cone: this would be consistent with a negative refraction behavior, which was found in this case to pertain predominantly to the collective excitation of the π electrons.

In a broader perspective, momentum-resolved STEM-VEELS allows for the determination of the confinement of individual modes in arbitrarily shaped nanostructures, where the required resolution in real and momentum space can be accurately controlled by the electron beam convergence. Fundamentally limited by the uncertainty relation and inelastic delocalization, it was found that, even at relatively poor momentum resolution, the presented technique provides clear evidence for localization. While dedicated EEL spectrometers and optical techniques allow for highly resolved momentum-dependent measurements averaged over relatively large areas of a sample, the STEM-VEELS technique used here provides a direct probe of localization and negative refraction at high spatial resolution. If combined with energy-filtered imaging or spectrum imaging experiments, this approach allows for highly versatile nanoscale characterization in the electron microscope for the development of novel plasmonic devices.

APPENDIX A: ZERO-LOSS PEAK REMOVAL AND PEAK FITTING

For an accurate determination of peak positions, the contribution of the ZLP must be removed. There is a large variety of ZLP removal techniques, from peak fitting routines to Fourier-space deconvolution, but no single technique is commonly accepted as a standard for all applications.[44] In the present case, the best compromise between noise levels and accuracy of the subtraction was obtained by removing the ZLP contribution using a power-law fit to the ZLP tail.

The success of applying this method is critically dependent on an accurate subtraction, as any deviation from the true profile could cause an error in spectral intensities of up to ∼6 eV.[45] All datasets were therefore processed with several techniques and the results cross-checked for consistency even though only the power-law fit results are discussed here. As any pure subtraction method, a simple power-law fit fails to remove plural scattering.[3] The effect of plural scattering could have been avoided if Fourier-log deconvolution[3] had been used. However, as this was found to significantly increase spectral noise, it was not used in the final analysis. Thus, plural scattering was taken into account by introducing an additional component in the peak fitting procedure, as described below.

Plasmon peak positions were determined by fitting four components corresponding to: (i) $\pi \rightarrow \pi^*$ interband transitions (and possibly some residual ZLP tail intensity); (ii) the π plasmon; (iii) the $\pi + \sigma$ plasmon; and (iv) plural scattering (PS), all on a linear background. Figure 3 shows an example of a fitted spectrum from the tip of P2 acquired with $q = 0 \pm 1.2$ Å^{-1}, where components (i)–(iv) are indicated. Here, components (i)–(iii) were assigned following the work of Reed and Sarikaya[45] on single-wall carbon nanotubes, neglecting surface mode contributions, while component (iv) accounted for plural scattering. In contrast to Ref. 45, pure Lorentzian peak profiles were not found to be a good representation of the peaks observed in the loss spectra. Good agreement was, however, found when using pseudo-Voigt (mixed Gaussian and Lorentzian) functions, the only exception being spectra acquired at high q values (e.g. $q = 1.3 \pm 1.2$ Å^{-1} and $q = 1.5 \pm 1.2$ Å^{-1}), where peaks were fitted with asymmetric Lorentzians to account for a significant peak broadening in this regime due to plasmon dampening.[46] All fits were converged fully by root-mean-square regression. Interestingly, the Gaussian-Lorentzian character required for an optimal peak fit was found to depend on convergence semiangle as well as particle shape. Disc spectra [P0(9 mrad), P0(4 mrad)] were fitted with a 75% Lorentzian character independent of convergence, while cones (P2, P5) were fitted with a 50% Lorentzian character for $\alpha = 9$ mrad, and P5 were fitted with a 75% Lorentzian for $\alpha = 4$ mrad. Reportedly, the functional form for exciting a single damped quantum harmonic oscillator can be estimated by a Lorentzian peak.[45] Thus, an increase in the Gaussian contribution in the peak profile of P5 might be attributed to an average over more Lorentzian oscillators in momentum space, effectively smearing the spectrum with increasing beam convergence. Similarly, the difference in peak shape between cones and discs might be explained by smearing, in this case attributed to an increased contribution of the out-of-plane components of the dielectric function.[7,42]

APPENDIX B: ERROR ESTIMATION

The statistical error in plasmon peak energy was estimated by $\pm\Delta E/\sqrt{N}$ given that $\Delta E \gg \delta E$, where ΔE is the peak width, N is the number of counts under the fitted peak, and δE is the energy spread per channel, where the approximation $\Delta E \gg \delta E$ is valid if the width of the peak is larger than ten times the energy spread/channel.[15] This was found to be the case for all plasmon peaks fitted, and the statistical error estimate consistently returned an average error of $\approx \pm 0.02$ eV for all measured structures—an order of magnitude smaller than δE. Note that the total error in plasmon energy is also dependent on the accuracy of the ZLP removal procedure as well as any error in peak-shape estimation. The error arising from the choice of a pseudo-Voigt peak shape was estimated by fitting spectra separately with both pure Gaussians and Lorentzian functions to full convergence by means of root-mean-square regression. The difference in fitted plasmon energy was then calculated for each spectrum, yielding an upper boundary for the uncertainty in energy loss due to the choice of peak shape of $\approx \pm 0.03$ eV for the π plasmon and $\approx \pm 0.15$ eV for the $\pi + \sigma$ plasmon. The error in the π plasmon energy is close to the statistical error, indicating low sensitivity to peak shape, while for the $\pi + \sigma$ plasmon, the estimate indicates a significant sensitivity to peak shape which can be attributed to the significant overlap with the plural scattering peak (Fig. 3). The tails of the pure Gaussian and Lorentzian functions consistently produced a significant mismatch to spectra, making them unrealistic alternatives to pseudo-Voigt fitting functions. Thus, the actual uncertainty due to choice of peak shape is expected to be far less than the upper estimate provided here, and significantly so for the $\pi + \sigma$ plasmon. From these considerations, a combined (nonstandard) error is estimated by adding errors in quadrature, yielding $\pm\sigma\,(E_\pi) \leqslant \pm 0.04$ eV and $\pm\sigma\,(E_{\pi+\sigma}) < \pm 0.15$ eV for the π and $\pi + \sigma$ plasmons, respectively. In addition, $\sigma\,(E_\pi)$ is expected to be sensitive to the accuracy of the ZLP tail removal procedure,[45] while no such effect is expected for $\sigma\,(E_{\pi+\sigma})$. Lastly, it is assumed that the error in estimating the asymmetric Lorentzian peak shape at $q = 1.3 \pm 1.2$ Å^{-1} and $q = 1.5 \pm 1.2$ Å^{-1} is comparable to that of the pseudo-Voigt fits. Estimated errors in energy loss as well as in momentum transfer (see Table I) are indicated in Figs. 7 and 8.

[*]Corresponding author: fshage@superstem.org

[1]S. A. Maier and H. A. Atwater, J. Appl. Phys. **98**, 011101 (2005).

[2]J. A. Dionne and H. A. Atwater, MRS Bull. **37**, 717 (2012).

[3]R. F. Egerton, *Electron Energy-Loss Spectroscopy in the Electron Microscope* (Springer, Berlin, 2011).

[4]T. A. Kelf, Y. Sugawara, R. M. Cole, J. J. Baumberg, M. E. Abdelsalam, S. Cintra, S. Mahajan, A. E. Russell, and P. N. Bartlett, Phys. Rev. B **74**, 245415 (2006).

[5]T. Pichler, M. Knupfer, M. S. Golden, J. Fink, and T. Cabioc'h, Phys. Rev. B **63**, 155415 (2001).

[6]T. Pichler, M. Knupfer, M. S. Golden, J. Fink, A. Rinzler, and R. E. Smalley, Phys. Rev. Lett. **80**, 4729 (1998).

[7]H. Raether, *Excitations of Plasmons and Interband Transitions by Electrons* (Springer-Verlag, New York, 1980).

[8]J. Daniels, C. v. Festenberg, H. Raether, and K. Zeppenfeld, in *Springer Tracts in Modern Physics*, Vol. 54 (Springer, Berlin/Heidelberg, 1970), p. 77.

[9] X. Liu, T. Pichler, M. Knupfer, M. S. Golden, J. Fink, D. A. Walters, M. J. Casavant, J. Schmidt, and R. E. Smalley, Synth. Met. **121**, 1183 (2001).

[10] R. F. Egerton, Ultramicroscopy **107**, 575 (2007).

[11] J. Wang, Q. Li, and R. F. Egerton, Micron **38**, 346 (2007).

[12] R. Erni and N. D. Browning, Ultramicroscopy **108**, 84 (2008).

[13] E. Najafi, A. P. Hitchcock, D. Rossouw, and G. A. Botton, Ultramicroscopy **113**, 158 (2012).

[14] C. H. Chen and J. Silcox, Phys. Rev. Lett. **35**, 390 (1975).

[15] Y. Y. Wang, S. C. Cheng, V. P. Dravid, and F. C. Zhang, Ultramicroscopy **59**, 109 (1995).

[16] A. Gloter, M.-W. Chu, M. Kociak, C. H. Chen, and C. Colliex, Ultramicroscopy **109**, 1333 (2009).

[17] M. K. Kinyanjui, C. Kramberger, T. Pichler, J. C. Meyer, P. Wachsmuth, G. Benner, and U. Kaiser, Europhys. Lett. **97**, 57005 (2012).

[18] C. Q. Qu, L. Qiao, C. Wang, S. Yu, W. T. Zheng, and Q. Jiang, IEEE T. Nanotechnol. **8**, 153 (2009).

[19] J. C. Charlier and G. M. Rignanese, Phys. Rev. Lett. **86**, 5970 (2001).

[20] F. S. Hage, D. M. Kepaptsoglou, Q. M. Ramasse, C. R. Seabourne, R. Brydson, A. E. Gunnæs, and G. Helgesen, Microsc. Microanal. **18**(Suppl. 2), 1540 (2012).

[21] D. L. Carroll, P. Redlich, P. M. Ajayan, J. C. Charlier, X. Blase, A. De Vita, and R. Car, Phys. Rev. Lett. **78**, 2811 (1997).

[22] O. V. Yazyev and S. G. Louie, Phys. Rev. B **81**, 195420 (2010).

[23] Y. Zhang, J.-P. Hu, B. A. Bernevig, X. R. Wang, X. C. Xie, and W. M. Liu, Phys. Rev. B **78**, 155413 (2008).

[24] I. A. Ovid'ko, Rev. Adv. Mater. Sci. **30**, 201 (2012).

[25] L. Feng, X. Lin, L. Meng, J.-C. Nie, J. Ni, and L. He, Appl. Phys. Lett. **101**, 113113 (2012).

[26] J. C. Charlier, Acc. Chem. Res. **35**, 1063 (2002).

[27] A. Krishnan, E. Dujardin, M. M. J. Treacy, J. Hugdahl, S. Lynum, and T. W. Ebbesen, Nature **388**, 451 (1997).

[28] L. Serra, F. Garcias, M. Barranco, N. Barberán, and J. Navarro, Phys. Rev. B **44**, 1492 (1991).

[29] G. V. Viktor, Soviet Physics Uspekhi **10**, 509 (1968).

[30] J. Yao, Z. Liu, Y. Liu, Y. Wang, C. Sun, G. Bartal, A. M. Stacy, and X. Zhang, Science **321**, 930 (2008).

[31] H. J. Lezec, J. A. Dionne, and H. A. Atwater, Science **316**, 430 (2007).

[32] J. A. Bakken, R. Jensen, B. Monsen, O. Raanes, and A. N. Wærnes, Pure Appl. Chem. **70**, 1223 (1998).

[33] F. S. Hage, Ø. Prytz, A. E. Gunnæs, G. Helgesen, and R. Brydson (unpublished).

[34] S. N. Naess, A. Elgsaeter, G. Helgesen, and K. D. Knudsen, Sci. Tech. Adv. Mater. **10**, 065002 (2009).

[35] S. Iijima, Nature **354**, 56 (1991).

[36] O. L. Krivanek, G. J. Corbin, N. Dellby, B. F. Elston, R. J. Keyse, M. F. Murfitt, C. S. Own, Z. S. Szilagyi, and J. W. Woodruff, Ultramicroscopy **108**, 179 (2008).

[37] O. L. Krivanek, N. Dellby, M. F. Murfitt, M. F. Chisholm, T. J. Pennycook, K. Suenaga, and V. Nicolosi, Ultramicroscopy **110**, 935 (2010).

[38] H. R. Daniels, PhD thesis, University of Leeds, 2003.

[39] R. Erni and N. D. Browning, Ultramicroscopy **104**, 176 (2005).

[40] A. B. Shah, Q. M. Ramasse, J. G. Wen, A. Bhattacharya, and J. M. Zuo, Micron **42**, 539 (2011).

[41] R. F. Egerton, Micron **34**, 127 (2003).

[42] A. G. Marinopoulos, L. Reining, V. Olevano, A. Rubio, T. Pichler, X. Liu, M. Knupfer, and J. Fink, Phys. Rev. Lett. **89**, 076402 (2002).

[43] W. Zhou, S. J. Pennycook, and J.-C. Idrobo, Ultramicroscopy **119**, 51 (2012).

[44] J. A. Aguiar, B. W. Reed, Q. M. Ramasse, R. Erni, and N. D. Browning, Ultramicroscopy **124**, 130 (2013).

[45] B. W. Reed and M. Sarikaya, Phys. Rev. B **64**, 195404 (2001).

[46] A. G. Marinopoulos, L. Reining, A. Rubio, and V. Olevano, Phys. Rev. B **69**, 245419 (2004).

[47] J. Hubbard, Proc. Phys. Soc. Section A **68**, 976 (1955).

[48] K. Zeppenfeld, Z. Phys. **243**, 229 (1971).

[49] U. Büchner, Phys. Status Solidi B **81**, 227 (1977).

[50] F. Bassani and G. P. Parravicini, Il Nuovo Cimento B **50**, 95 (1967).

[51] H. Venghaus, Phys. Status Solidi B **66**, 145 (1974).

[52] N. M. B. Perney, J. J. Baumberg, M. E. Zoorob, M. D. B. Charlton, S. Mahnkopf, and C. M. Netti, Opt. Express **14**, 847 (2006).

[53] C.-W. Chiu, F.-L. Shyu, M.-F. Lin, G. Gumbs, and O. Roslyak, J. Phys. Soc. Jpn. **81**, 104703 (2012).